 CMC, vol.51, no.3, pp.145-161, 2016

Higher-Order Line Element Analysis of Potential Field with Slender Heterogeneities

H.-S. Wang[1,2], H. Jiang[3,4], B. Yang[2]

Abstract: Potential field due to line sources residing on slender heterogeneities is involved in various areas, such as heat conduction, potential flow, and electrostatics. Often dipolar line sources are either prescribed or induced due to close interaction with other objects. Its calculation requires a higher-order scheme to take into account the dipolar effect as well as net source effect. In the present work, we apply such a higher-order line element method to analyze the potential field with cylindrical slender heterogeneities. In a benchmark example of two parallel rods, we compare the line element solution with the boundary element solution to show the accuracy as a function in terms of rods distance. Furthermore, we use more complicated examples to demonstrate the capability of the line element technique.

Keywords: Electrostatics; Heat conduction; Integral equation technique; Line element method; Mesh reduction method, Potential field problems.

1 Introduction

Potential field problems described by Laplace (and generally, Poisson) equation are important in many areas such as thermal conduction, potential flow, and electrostatics [Telles and Wrobel (1984); Liu (2009)]. Very often slender bodies (i.e., heterogeneities) are involved, such as nanowires in nano- and micro-electro-mechanical systems, [Chen, Mukherjee, and Aluru (2008); Shen (2009)] and nanotube and glass fibers in composite materials [Nishimura and Liu (2004); Wang and Yao (2013); Chen and Mukherjee (2006); Fiamegkou, Athanasopoulos, and Kostopoulos (2014); Han and Fina (2011)]. Many biological materials such as protein, [Simonson (2003); Grochowski and Trylska (2008)] collagens and fibrins, [Dong

[1] School of Optoelectronics Beijing Institute of Technology, Beijing 100081, China
[2] Department of Mechanical and Aerospace Engineering, University of Texas at Arlington Arlington, TX 76019, USA
[3] State Key Laboratory of Digital Manufacturing Equipment and Technology, Huazhong University of Science and Technology, Wuhan, HuBei 430074, China
[4] Corresponding author E-mail: hjiang@hust.edu.cn

(2009); Jiang, Yang, and Liu (2013)] and solvated biomolecular system [Lu (2008)] fall in this class as well. The computational analysis of a system of slender bodies poses great challenge due to the high aspect ratio. The literature has seen scarce computational work on the potential field analysis with slender bodies despite its importance, likely due to difficulties arising from the high aspect ratio.

Finite difference (FD) method [Mitchell and Griffiths (1980)] and finite element (FE) method [Reddy and Gartling (2011)] are popular domain-based numerical techniques. By them, the domain is discretized into grids/elements, and a field over the domain is approximated piecewise with basis functions (such as polynomials) over local grids/elements. They are versatile, capable of dealing with virtually any physical problems. However, when they are applied to solve slender-body problems, a fine grid/mesh is required to reasonably resolve the characteristics of a slender body and its surrounding domain. Even if an adaptive mesh is used, the computational task can be prohibitively large. Boundary element (BE) method is another popular numerical technique. It is derived from a boundary integral equation and only involves numerical discretization on the boundary of a domain. The dimensionality reduction from a domain to a surface, typically by applying analytical integral kernels, is advantageous compared to the FD and the FE methods. However, the resulting stiffness matrix is full in contrast to the sparse matrix of the FD and the FE methods. When it is applied to solve slender-body problems, the computational task remains prohibitively large. In order to effectively and accurately solve slender-body problems, further mesh reduction is required. For potential field problems, [Chen and Mukherjee (2006)] introduced a line integral equation model summing the surface charge density around a slender heterogeneity into a line charge density meanwhile neglecting higher-order terms, such as line dipole density due to uneven charge distribution around the perimeter. On the other hand, such higher-order effect may become significant when the material property mismatch between the slender body and the surrounding medium is significant or when slender bodies closely interact with each other or with other objects. A line integral equation formulation has been applied to the hydrodynamics of a slender body with only side net force density [Pozrikidis (2011); Tornberg and Shelley (2004)] and with both net force and moment densities [Jiang, Wu, Zhao, and Yang (2014); Jiang and Yang (2013)]. In the present work, we introduce a higher-order line integral equation technique for potential field problems with slender heterogeneities, examine its efficiency and accuracy, and examine the characteristics of the potential field around a slender body.

The rest of the paper is organized as follows. In Sec. 2, we derive the line integral equations of potential field from the general boundary integral equations along a slender body by expanding the integral kernels in Taylor series about the slender

body central line and retaining the first two integral terms plus a finite term. The finite terms of a cylinder are derived, which carry the local information of a cross-sectional shape and represent the core structure behind the singularities. In Sec. 3, the numerical treatments to the line integral equation formulation are discussed. In Sec. 4, four examples are presented to demonstrate the capability and validity of the present method, in the context of steady-state heat conduction. They are: (a) temperature distribution along two parallel rods, both sources; (b) temperature distribution along two parallel rods, one source and the other sink; (c) temperature distribution along a spiral rod; (d) temperature distribution along a three-dimensional (3D) architecture of rods. In the cases of two parallel rods, the problem is examined with their distance as the parameter to show when the dipolar term is important and when the line model is accurate. In Sec. 5, conclusions are drawn.

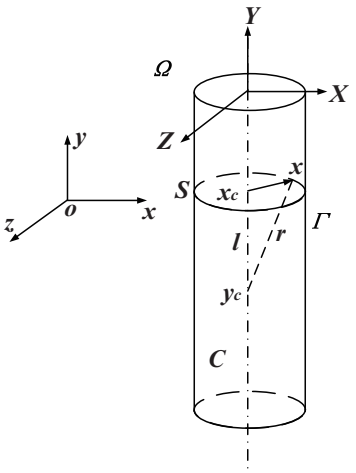

Figure 1: Schematic of two parallel rods with separation distance.

2 Line integral equations of potential field around a slender heterogeneity

2.1 Line integral equations along a slender cavity

Consider a problem of a scalar potential field around a slender cavity C in a domain Ω, as shown in Fig. 1. The fixed Cartesian coordinate system (x_1, x_2, x_3; O) is established for reference. Meanwhile, a Cartesian body frame (X_1, X_2, X_3; $\boldsymbol{x}^c$) is established with the second axis directed along the longitudinal direction and the normal axes residing within a cross section, and origin $\boldsymbol{x}^c$ being the centroid of the same cross section, of C. A lower-case subscript index will be used to indicate a component in the global frame, while an upper-case subscript index to indicate a

component in the body frame. Whenever a numerical number or a Greek letter is used to indicate a component, it refers to the body frame. (x, y, z) and (X, Y, Z) may also be used to indicate the components, in the global and the body frames, respectively, and they should not be confused with their bold-faced or indexed counterpart of a vector or a component of a vector.

The scalar potential field T satisfies the Laplace equation, $\nabla^2 T = 0$, within Ω. By applying the reciprocal theorem, the following boundary integral equation can be derived as

$$c(\boldsymbol{y})\,T(\boldsymbol{y}) = \int_{\Gamma} [T^*(\boldsymbol{y},\boldsymbol{x})\,J(\boldsymbol{x}) - J^*(\boldsymbol{y},\boldsymbol{x})\,T(\boldsymbol{x})]\,d\Gamma(\boldsymbol{x}), \tag{1}$$

where Γ is the boundary of Ω (including the surface of cavity C and a possible external surface if Ω is finite), $J \equiv -\boldsymbol{\nabla} T \cdot \boldsymbol{n}$, and $\boldsymbol{n}$ is the outward unit vector at a point on Γ. Constant $c = 1$ if $\boldsymbol{y} \in \Omega$; $= 1/2$ if $\boldsymbol{y} \in \Gamma$; $= 0$ if $\boldsymbol{y} \in C$. Integral kernels T^* and J^* are the fundamental solutions satisfying $\nabla^2 T^* + \delta = 0$ and $J^* \equiv -\boldsymbol{\nabla} T^* \cdot \boldsymbol{n}$, where δ is the Dirac delta function representing a point source, in an infinite space. They are given in terms of source point $\boldsymbol{y}$ and field point $\boldsymbol{x}$ by

$$T^*(\boldsymbol{y},\boldsymbol{x}) = \frac{1}{4\pi r} \text{ and } J^*(\boldsymbol{y},\boldsymbol{x}) = \frac{r_{,n}}{4\pi r^2}, \tag{2}$$

where $r = \boldsymbol{y} - \boldsymbol{x}$, and $r_{,n} = \dfrac{\partial r}{\partial \boldsymbol{x}} \cdot \boldsymbol{n}$.

In order to derive the corresponding line integral equation, let us approximate the potential field along the perimeter of a cross section of the slender cavity as

$$T(\boldsymbol{x}) = T^a(\boldsymbol{x}^c) + T^a_{,i}(\boldsymbol{x}^c)\,\rho_i + o\left(\rho^2\right). \tag{3}$$

where $\boldsymbol{\rho} = \boldsymbol{x} - \boldsymbol{x}^c$, $\rho = |\boldsymbol{\rho}|$, the subscript comma is reserved to denote the partial differentiation with respect to the index that follows and the repeated index indicates the Einstein convention of summation. T^a should be understood as the average potential on the perimeter. Meanwhile, $T^a_{,j}$ should be understood as the difference of potential across the cross section (normalized by the distance) along jth axis, i.e., the nominal gradient of potential along the perimeter. They are assigned to centroid $\boldsymbol{x}^c$ to merely indicate that they belong to the cross section centered at $\boldsymbol{x}^c$. By setting $\boldsymbol{y}$ to be on the center line of the slender cavity (hence $\boldsymbol{y} \in C$), and truncating Eq. (3) at the linear order and substituting it to the second term on the right-hand side of Eq. (1), we obtain

$$\begin{aligned} &\int_{\Gamma^{sc}} J^*(\boldsymbol{y}^c,\boldsymbol{x}) \left(T^a(\boldsymbol{x}^c) + T^a_{,i}(\boldsymbol{x}^c)\,\rho_i\right) d\Gamma(\boldsymbol{x}) \\ &= \int_{\Gamma^{sc}} T^*(\boldsymbol{y}^c,\boldsymbol{x})\,J(\boldsymbol{x})\,d\Gamma(\boldsymbol{x}) + T^{ex}(\boldsymbol{y}^c), \end{aligned} \tag{4a}$$

$$T^{ex}(\boldsymbol{y}^c) = \int_{\Gamma^{ex}} T^*(\boldsymbol{y}^c,\boldsymbol{x}) J(\boldsymbol{x})\, d\Gamma(\boldsymbol{x}) - \int_{\Gamma^{ex}} J^*(\boldsymbol{y}^c,\boldsymbol{x})\, T(\boldsymbol{x})\, d\Gamma(\boldsymbol{x}), \tag{4b}$$

where Γ^{sc} is the slender cavity boundary, and Γ^{ex} is the external boundary. Examining it in the vicinity of $\boldsymbol{y}^c$, one may realize that the term on the left-hand side of Eq. (4a) is equal to $T(\boldsymbol{y}^c)$ plus residual on the order of ρ^2/L^2, where L is a characteristic length scale, for instance, the radius of curvature of the slender cavity, the distance between the slender body and an external boundary, and the distance between slender bodies if there are multiple of them – whichever is the smallest. Thus, the above equation may be rewritten as

$$T(\boldsymbol{y}^c) = \int_{\Gamma^{sc}} T^*(\boldsymbol{y}^c,\boldsymbol{x}) J(\boldsymbol{x})\, d\Gamma(\boldsymbol{x}) + T^{ex}(\boldsymbol{y}^c). \tag{5}$$

We then expand T^* in Taylor series (up to the linear term) in the vicinity of $\boldsymbol{x}^c$ and use it to approximate Eq. (5) as

$$\begin{aligned} T(\boldsymbol{y}^c) =& T^{ft}(\boldsymbol{y}^c) + \int_{\Gamma} \left[T^*(\boldsymbol{y}^c,\boldsymbol{x}^c) J(\boldsymbol{x}) + T^*_{,i}(\boldsymbol{y}^c,\boldsymbol{x}^c)\, \rho_i(\boldsymbol{x}) J(\boldsymbol{x}) \right] \\ & d\Gamma(\boldsymbol{x}) + T^{ex}(\boldsymbol{y}^c), \end{aligned} \tag{6}$$

where the integrals are taken in the sense of Cauchy or Hadamard principal value depending on the odd or even order of a singularity in the kernels, and T^{ft} is a finite term resulting from the limiting process of $\boldsymbol{x}^c \to \boldsymbol{y}^c$. By realizing that the integral kernels are now independent of local circumferential direction (s) of a cross section, we rewrite Eq. (6) as

$$T^a = T^{ft} + \int_l \left[T^* Q + T^*_{,i} D_i \right] dl + T^{ex}, \tag{7}$$

where $Q(\equiv \oint J ds)$ is the net source density per unit length, and $D_i(\equiv \oint J \rho_i ds)$ is the source dipole density per unit length, derived from the distributed sources on a perimeter. Q is conjugate with potential T^a, and D_i is conjugate with nominal potential gradient $T^a_{,i}$. Thus, we have derived the line integral equation of potential along center line l for a slender cavity based on the generic boundary integral equation that makes no assumption b beyond Laplace's equation.

In order to complete the formulation, higher-order integral equations are required. By taking derivative of all terms in Eq. (1) with respect to source point $\boldsymbol{y}$, and following the same procedure of derivation as above, we can obtain the line integral equation of potential gradient. For the sake of brevity, the derivation is omitted. This equation is given by

$$T^a_{,p} = T^{ft}_{,p} + \int_l \left[T^*_{,p} Q + T^*_{,ip} D_i \right] dl + T^{ex}_{,i}. \tag{8}$$

The above equations (7) and (8) are termed as the dual line-integral equations for perimeter-average potential T^a and nominal potential gradient $T^a_{,p}$ at a slender cavity. They are accurate on the order of ρ/L, with higher-order terms neglected. The loading terms of net source and source dipole are taken into account. In the following, we shall fill the slender cavity with a slender body so that the above line integral equations can be further reduced.

2.2 Line integral equation formulation of a slender heterogeneity

Let us fill in the above slender cavity C with a heterogeneity H of the same shape. The potential field inside H is modeled as one-dimensional, and is characterized by using average potential T^H and nominal gradients $T^H_{,1}$ and $T^H_{,2}$ along local axes X and Y over a cross section, along central line l. The conjugate loading terms are correspondingly heat source and dipoles, Q^H, D^H_1 and D^H_2, defined over a cross section. By assuming the continuity conditions of both potential and source fields across the interface between the heterogeneity and surrounding medium, and substituting the heterogeneity fields in Eqs. (7) and (8), we have

$$T^H = T^{ft} + \int_l \left[T^* Q^H + T^*_{,\alpha} D^H_\alpha\right] dl + T^{ex}, \tag{9}$$

$$T^H_{,\beta} = T^{ft}_{,\beta} + \int_l \left[T^*_{,\beta} Q^H + T^*_{,\alpha\beta} D^H_\alpha\right] dl + T^{ex}_{,\beta}, \tag{10}$$

where α and β range from 1 to 2, representing X and Y in the body frame.

2.3 Finite terms

The line integrals in Eqs. (6)–(10) are singular when the source and field points coincide. They are taken in the sense of Cauchy or Hadamard principal value depending on their odd or even order. It means that these line integrals do not contain any physical information inside the core of the singularity, such as the cross-sectional shape and the interfacial continuity condition. Thus, it must be added back to the line-integral equations to represent the physics correctly. In light of this understanding, these finite terms are defined as

$$T^{ft} = \int_{\Gamma^{sc}} T^* J d\Gamma - \int_l \left[T^* Q + T^*_{,\alpha} D_\alpha\right] dl, \tag{11}$$

$$T^{ft}_{,\beta} = \int_{\Gamma^{sc}} T^*_{,\beta} J d\Gamma - \int_l \left[T^*_{,\beta} Q + T^*_{,\alpha\beta} D_\alpha\right] dl. \tag{12}$$

In the present work, we specify the slender cavity C (and hence, the matching heterogeneity H) to be of a circular cross section. Also, it is assumed that the central line l is only slightly curved so that it can be reasonably approximated as

straight locally at its any middle location. Under these conditions, the finite terms, T^{ft}, $T^{ft}_{,1}$ and $T^{ft}_{,2}$ can be derived. We have analytically integrated over an infinite slender cavity and obtained the following results:

$$T^{ft} = \frac{1}{2\pi}(\ln 2 - \ln R)\, Q^H, \tag{13}$$

$$T^{ft}_{,\alpha} = \frac{1}{2\pi R^2} D^H_\alpha, \tag{14}$$

where R is the radius of the circular cross section. Assigning Q and D_α to slender heterogeneity, it was implied that the fields are continuous across the interface.

3 Numerical line element method

In this section, we introduce a numerical scheme to solve the problem of potential field with a slender heterogeneity as formulated above. A slender heterogeneity, modeled as a line object, is discretized by using piecewise straight elements. A single node is placed at the middle point of each element. Each node is associated with 3 degrees of freedom, average potential T^H, and nominal potential gradient within a cross-sectional plane, $T^{ft}_{,\beta}$, for $\beta = 1, 2$. The discretized versions of Eqs. (9) and (10) are given by

$$T^{H(n)} = T^{ft(n)} + \sum_{m=1}^{N} \left[\hat{T}^{*(nm)} Q^{H(m)} + \hat{T}^{*(nm)}_{,\alpha} D^{H(m)}_\alpha \right] + T^{ex(n)}, \tag{15}$$

$$T^{H(n)}_{,\beta} = T^{ft(n)}_{,\beta} + \sum_{m=1}^{N} \left[\hat{T}^{*(nm)}_{,\beta} Q^{H(m)} + \hat{T}^{*(nm)}_{,\alpha\beta} D^{H(m)}_\alpha \right] + T^{ex(n)}_{,\beta}, \tag{16}$$

where superscript n/m denotes the nth/mth node, and N is the total number of nodes. The nodal finite terms are: $T^{ft(n)} = \frac{1}{2\pi}(\ln 2 - \ln R)\, Q^{H(n)}$, and $T^{ft(n)}_{,\alpha} = \frac{1}{2\pi R^2} D^{H(n)}_\alpha$, in which R is taken to be the slender-body radius at the nth node. Note that only a remote external boundary is considered here whose corresponding terms, if any, are treated as prescribed.

The influence coefficients $\hat{T}^{*(nm)}$, $\hat{T}^{*(nm)}_{,\alpha}$, $\hat{T}^{*(nm)}_{,\beta}$, and $\hat{T}^{*(nm)}_{,\alpha\beta}$ are line integrals of corresponding fundamental solutions over the element of the mth node. For example, $\hat{T}^{*(nm)} = \int_{l^{(m)}} T^*(\boldsymbol{y}^{c(n)}, \boldsymbol{x}^c) dl(\boldsymbol{x}^c)$. These line integrals along a straight line can all be analytically obtained; for the sake of brevity, they are not presented here.

Finally, we can apply Eqs. (15) and (16) to solve for nodal potential quantities or corresponding loading sources, whichever are unknown, given the other. In the following section of numerical examples, we shall only consider such a case. If these fields are all unknown, for instance, if the slender heterogeneity is itself conductive and of a finite conductivity in the case of heat condition, another set of equations

based on the physical process within the slender heterogeneity would be derived to complete the formulation for a unique solution; we leave this consideration to future studies. In converting Eqs. (9) and (10) to Eqs. (15) and (16), the only numerical parameter is the element size. Similar to the hydrodynamic case, we have found convergence of numerical results with mesh refinement, except the following note. Since the finite terms (Eqs. (13) and (14)) are for interior nodes, the end effect of a slender heterogeneity has not been captured in the present work. We need to use a long enough element at the ends to avoid computational instability that may occur otherwise. We leave it for future consideration to derive the finite terms for an end node due to a semi-infinite line source.

4 Numerical examples

In this section, the proposed LE method is demonstrated by using examples in heat conduction. At first, the case of two parallel rods with identical, higher temperature in an infinite medium is used as a benchmark problem to demonstrate the validity of the method. By the process of retrieving the local information, more physical interpolations of the finite terms are given. It demonstrates that the proposed LE method is valid at the slender heterogeneity limit compared to the BE method. In order to further show the capability of the proposed LE method, three more applications of (b) two anti-symmetric parallel rods with separation distance; (c) a helical rod; and (d) 3-dimentional cross architecture of rods in a temperature field, are discussed. Compared with the BE solution, the LE solution is shown to be valid and far more efficient, which can be expected as a powerful tool for the study of potential field problems.

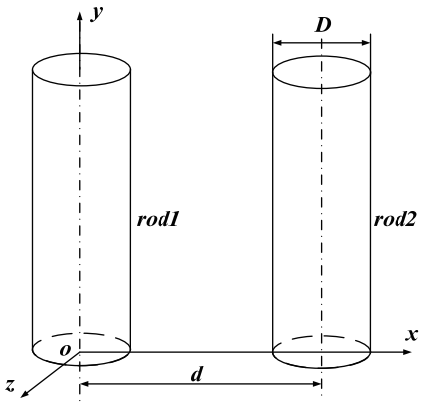

Figure 2: Schematic of two parallel rods with separation distance.

4.1 Two parallel rods, both sources

Two parallel rods as shown in Fig. 2 are used in the first case study. In this case, the remote temperature is set to be zero, i.e. $T_\infty = 0$. The temperature of both rods is specified as one unit, representing a symmetric condition. The rod radius a is used as the characteristic length scale and the length of each rod is 100 times of that. Thus, the high aspect ratio satisfies the slender body assumption. For the purpose of validity demonstration of the proposed LE method, the BE method is used to provide a baseline solution in this case.

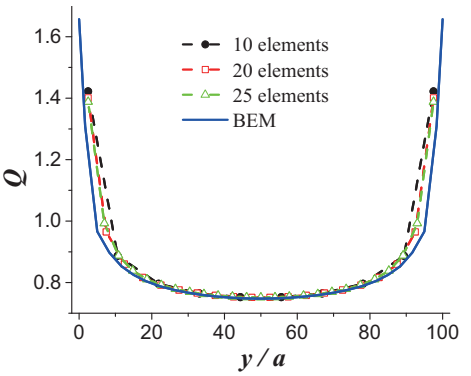

Figure 3: Variation of heat flux along a slender rod, predicted with various mesh densities.

For the case of rod separation distance $d = 3a$, the LE results of heat flux along the rod obtained with 10, 20, 25 elements are shown in Fig. 3. The corresponding BE result is also shown, which is due to a mesh of 100 equal divisions in length, 24 equal divisions in circumference, and 5 equal divisions in radius, over the rod surface. This mesh was checked to yield converged BE solutions. The results presented in Fig. 3 show that the solutions of LE method are stable and agree with the results obtained by using the BE method.

Secondly, we examine the separation distance dependence of the LE solution. Figures 4(a) and (b) show the heat flux and flux gradient, respectively, when the separation distance between the two rods are $3a$, $5a$, and $9a$. The results show excellent agreement between the LE and BE solutions, especially when the separation distance is relatively large. As shown in Fig. 4(a), the heat flux on the two rods are the same, exhibiting the symmetry. When the separation distance is decreasing, the value of the heat flux decreases. As shown in Fig. 4(b), the heat flux nonuniformality around the rod perimeter becomes larger when they get close to each other.

Upon the above mesh and separation distance dependence analysis, we present

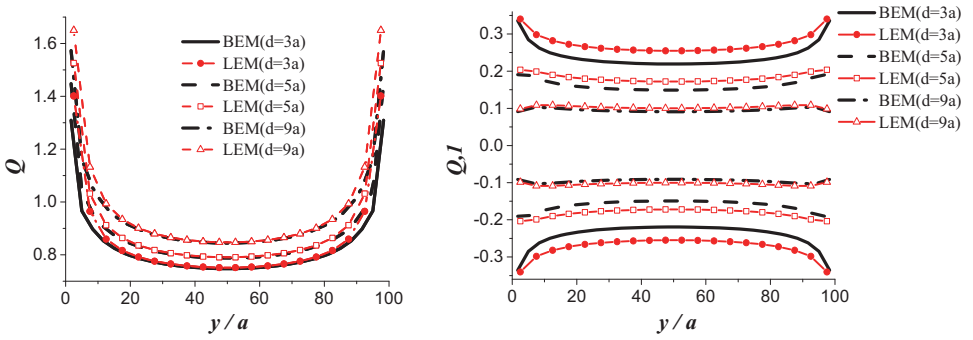

(a) (b)

Figure 4: (a) Variation of heat flux (Q) and (b) Variation of heat flux gradient (Q, 1) around two slender rods, at separation distance $d = 3a$, $5a$ and $9a$.

some detailed results for further analysis and discussion. Recalling in the process of line integral derivation, the net source and source dipole are the integrations along the perimeter of the cross-section, we are able to retrieve the local information by curve fitting using the least square (LSQ) method. Let us assume that the local heat flux can be expressed as

$$J_n = J_0 + a\cos(\varnothing) + b\sin(\varnothing), \tag{17}$$

where J_n is the total heat flux at a specific position on the center line of the slender body; $J_0 = \oint J_n ds = (J_1 + J_2)/2$; a and b are constants, which can be interpolated as $a = \oint J_n k_a \cos\varnothing d\varnothing$ and $b = \oint J_n k_b \sin\varnothing d\varnothing$, respectively; $\varnothing$ is the azimuth angle ranging from 0 to 2π. If the position of y is specified as the middle point on the center line of the rod, the curve fitting results and corresponding residual errors for different separation distances between the two rods are shown in Fig. 5(a) and (b). The parameters for curve fitting are listed in Table 1.

Meanwhile, the second order non-linear curve fitting to the full solution is tested, which is expressed by

$$J_n = J_0 + a\cos(\varnothing) + b\sin(\varnothing) + c\cos(2\varnothing) + d\sin(2\varnothing), \tag{18}$$

where c and d are additional constants, which can be interpolated as $c = \oint J_n k_c \cos 2\varnothing d\varnothing$ and $d = \oint J_n k_d \sin 2\varnothing d\varnothing$, respectively. The curve fitting results and corresponding residual errors for various separation distances between the two rods are shown in Figs. 6(a) and (b), respectively. The parameters obtained from the curve fitting are listed in Table 2.

As shown in Figs. 5 and 6, both of the first-order and second-order curve fittings can fit the local heat flux qualitatively well. It indicates that the local information

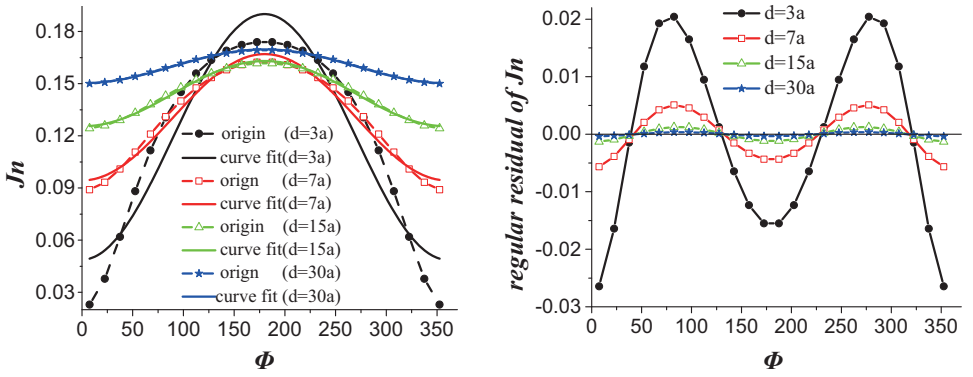

(a) (b)

Figure 5: The first order nonlinear curve fit result.

Table 1: First order nonlinear curve fit parameters result.

d value		Value	Standard Error
3	$\boldsymbol{J}_0$	0.11942	0.00327
	a	−0.07062	0.00463
	b	−1.49E-13	0.0046
7	$\boldsymbol{J}_0$	0.13068	7.93E-04
	a	−0.03633	0.00112
	b	9.98E-13	0.00112
15	$\boldsymbol{J}_0$	0.14426	1.97E-04
	a	−0.01878	2.78E-04
	b	−1.91E-15	1.17E-04
30	$\boldsymbol{J}_0$	0.15999	5.48E-05
	a	−0.00971	7.74E-05
	b	−2.47E-16	0

dropped in the integration reduction can be retrieved if the geometry of the cross-section is known. When the two rods are far enough away from each other, the high-order term can be neglected, and the first order term can be used attaining enough numerical accuracy. When the separation distance decreases, the fitting results deviate from the full solution, as may be expected. This is because the high order terms become more significant as the two rods get close to each other. By comparing the results in Figs. 5(a) and Fig. 6(a), it can be seen that when the separation distance is comparable to the diameter of the rod, the high order curve fitting gives more accurate fitting results, suggesting that the higher-order term (>

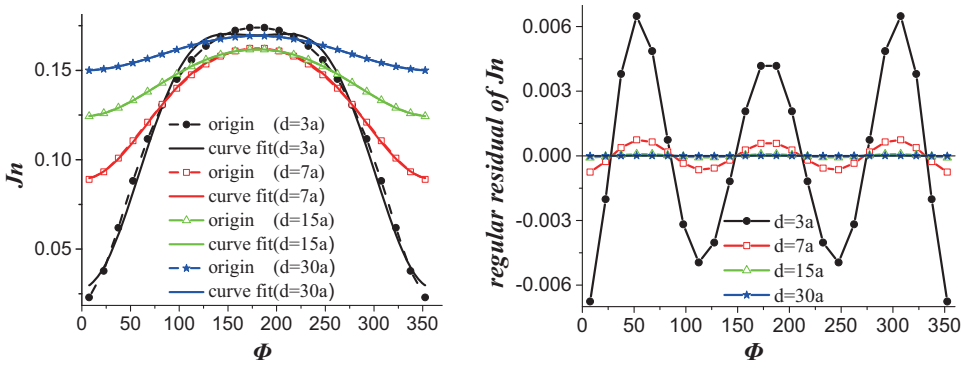

(a) (b)

Figure 6: The second order nonlinear curve fit result.

Table 2: Second order nonlinear curve fit parameters result.

d value		Value	Standard Error
3	$\boldsymbol{J}_0$	0.11942	9.47E-04
	a	−0.07062	0.00134
	b	3.50E-16	0
	c	−0.02038	0.00134
	d	−7.97E-16	8.42E-04
7	$\boldsymbol{J}_0$	0.13068	1.17E-04
	a	−0.03633	1.65E-04
	b	−3.35E-15	1.05E-04
	c	−0.00509	1.65E-04
	d	3.21E-15	2.45E-04
15	$\boldsymbol{J}_0$	0.14426	1.37E-05
	a	−0.01878	1.94E-05
	b	1.14E-14	1.83E-05
	c	−0.00127	1.94E-05
	e	9.88E-15	2.52E-05
30	$\boldsymbol{J}_0$	0.15999	1.93E-06
	a	−0.00971	2.73E-06
	b	2.10E-15	0
	c	−3.55E-04	2.73E-06
	d	−2.52E-15	1.52E-06

dipole) should be considered to achieve higher quantitative accuracy.

4.2 Two parallel rods, one source and the other sink

In the second example, the thermal distribution of two anti-symmetric parallel rods with various separation distances is analyzed. The geometry of both rods is the same as in the above case. The heat flux condition is prescribed with $Q = 1$ unit on one rod and $Q = -1$ unit on the other. They represent a source and a sink, respectively. No dipole is prescribed on either rod. The LE results of temperature and temperature gradient along the two rods obtained with 20 elements for selected separation distance are shown in Fig. 7.

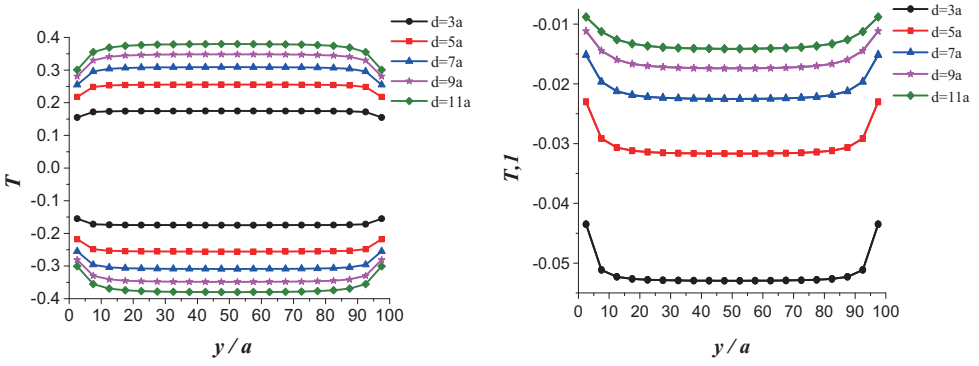

(a) (b)

Figure 7: (a) Variation of temperature (T) and (b) temperature gradient (T, 1) distribution around the two anti-symmetry rods when $d = 3a$, $5a$, $7a$, $9a$, $11a$.

As shown in Fig. 7(a), the temperature on the two rods have the same value but different signs, exhibiting the skew symmetry. When the separation distance is small, the absolute value of the temperature approaches to zero. When they get close to each other, the source and sink of equal intensity basically annihilate. As shown in Fig. 7(b), the temperature nonuniformality around the rod perimeter is trivial when the rods are far away from each other but becomes significant when they get close to each other. It might be worth noting that if the rods are thermoelastic, they would bend due to the varying temperature around the surface and inside the rods.

4.3 A helical rod

In the third case study, a helical rod as shown in Fig. 8 is considered. The helical rod is of radius R, and of a center-line shape defined by

$$x = c_1\varphi\cos(\varphi), \quad y = c_2\varphi\sin(\varphi), \quad z = c_3\varphi \tag{19}$$

where φ is the azimuth angle, (x,y,z) are the coordinates in the global coordinate system, and c_1, c_2 and c_3 are the constants. Here $c_1 = c_2 = R$, $c_3 = 50R$ and

$\varphi = [0, 6\pi]$ are used. A uniform heat flux Q equal to one unit is applied through the helix. The spiral slender body is discretized into 90 segments and each segment is treated as a straight rod. The line represents the helical rod, and the black solid dots show the nodes. The LE solution is superimposed on the rod curve, as shown in Fig. 8. Each arrow starts from the location of a node, and the end of the arrow is at $(x+T_{,1x}, y+T_{,1y}, z+T_{,1z})$. It represents the calculated temperature "gradient" at the specific position and illustrates the temperature nonuniformity. It can be seen that the temperature gradient vectors (i.e., arrows) along the solid surface imply that the heat is released more into the center of the spiral.

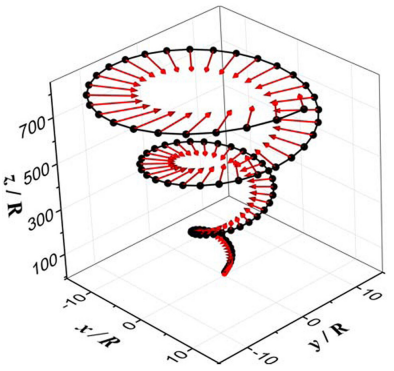

Figure 8: A slightly curved slender spiral. The dots show the nodes used in the simulation and the arrows represent the predicted temperature gradient vectors along the spiral when heat flux is considered as a constant.

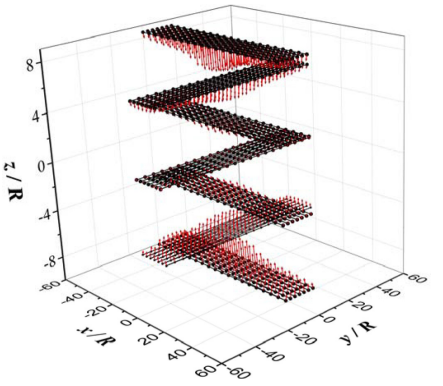

Figure 9: A 3d architecture of rods. The dots show the nodes used in the simulation and the arrows represent the predicted temperature gradient vectors along the spiral when heat flux is considered as a constant.

4.4 A 3D architecture of rods

A 3D cross architecture of rods in a temperature field is discussed in the fourth case. The rods in a layer are overlapped with right angles to the rods in the neighboring layers, which is defined by

$$\begin{cases} x = c_1 \cos(\varphi_x) \\ y = c_2 \cos(\varphi_y) \\ z = c_3 \cos(\varphi_z) \end{cases}$$

where φ_x, φ_y and φ_z are the azimuth angles along x axis, y axis and z axis, separately. (x, y, z) are the coordinates in the global coordinate system, and c_1, c_2 and

c_3 are the constants. Here $c_1 = c_2 = c_3$. $\varphi_y = \varphi_x + \pi/2$, $\varphi_z = \pi/2$. The geometry of the $3d$ cross architecture of rods is presented in Fig. 14. The $3d$ cross architecture is stacked by 7 layers of lattices separated by the distance of 3. Each layer consists of 7 parallel rods and the neighboring rods are separated by the distance of 3. Each cross rod is discretized into 20 segments. The line with solid dots represents the 3D cross architecture of rods, and the black solid dots show the nodes as shown in Fig.9.

When heat flux is assumed as a constant ($Q = 1$), the LE result of temperature gradient $(T,1)$ distributed on the 3D cross architecture of rods in global frame is shown in Fig. 9. As shown in this figure, the temperature gradient vectors (i.e., arrows) of the cross architecture rods imply heat releasing into the center of 3D cross architecture. The amplitude of the temperature gradient is decreasing from the outer layer to the center layer but for each rod, the amplitude of the temperature gradient is increasing from the ends to its middle point.

5 Conclusion

We have presented a numerical analysis of the potential field problem by applying a second-order LE method. The LE method is generally a mesh reduction method further from the BE method, specially devised for slender heterogeneities. The derivation is rigorous by reducing from the boundary integral equation. It can be applied to obtain the potential difference and flux difference (dipole) on opposing sides of a slender heterogeneity as well as the average potential and total flux around it. Such higher-order terms can be important when to study close interaction of slender heterogeneities with walls and with themselves. In particular, we have examined in detail the benchmark case of two parallel rods by comparing the LE and the BE solutions. The parameterized LE solution is reconstructed by using sinusoidal functions. The reconstructed fields agree with the BE solution well when the rods distance is large (compared to the rod radius). They become different when the rods get very close to each as expected. This comparative study demonstrates the validity of the present LE method. Furthermore, three more examples are presented to demonstrate the capability of the present LE method, including a long spiral heterogeneity and a 3D cross architecture of rods emitting heat. The present LE method may find itself for various applications in MEMS, fiber composites, etc. involving slender heterogeneities.

Acknowledgement: This work is sponsored by the State Scholarship Fund from the China Scholarship Council (CSC), whose support (Grant No. 201203070476) is gratefully acknowledged.

References

Chen, H.; Mukherjee, S. (2006): Charge distribution on thin conducting nanotubes – reduced 3-D model. *International Journal for Numerical Methods in Engineering*, vol. 68, no. 5, pp. 503–524.

Chen, H.; Mukherjee, S.; Aluru, N. (2008): Charge distribution on thin semiconducting silicon nanowires. *Computer Methods in Applied Mechanics and Engineering*, vol. 197, no. 41, pp. 3366–3377.

Dong, B. (2009): Electrospinning of collagen nanofiber scaffolds from benign solvents. *Macromolecular Rapid Communications*, vol. 30, no. 7, pp. 539–542.

Fiamegkou, E.; Athanasopoulos, N.; Kostopoulos, V. (2014): Prediction of the effective thermal conductivity of carbon nanotube-reinforced polymer systems. *Polymer Composites*, vol. 35, no. 10, pp. 1997–2009.

Grochowski, P.; Trylska, J. (2008): Continuum molecular electrostatics, salt effects, and counterion binding – a review of the Poisson-Boltzmann theory and its modifications. *Biopolymers*, vol. 89, no. 2, pp. 93–113.

Han, Z.; Fina, A. (2011): Thermal conductivity of carbon nanotubes and their polymer nanocomposites: a review. *Progress in Polymer Science*, vol. 36, no. 7, pp. 914–944.

Jiang, H.; Wu, Y. T.; Zhao, Y.-P.; Yang, B. (2014): Force-moment line element method for Stokes flow around a slender body. *Engineering Analysis with Boundary Elements*, vol. 44, pp. 120–129.

Jiang, H.; Yang, B. (2013): Force-moment line element method for flexible slender bodies in Stokes flow. *Physical Review E*, vol. 88, no. 3.

Jiang, H.; Yang, B.; Liu, S. (2013): Effects of transverse shear on strain stiffening of biological fiber networks. *CMC: Computers, Materials & Continua*, vol. 38, no. 2, pp. 61–77.

Liu, Y. (2009): Fast multipole boundary element method: theory and applications in engineering, Cambridge university press.

Lu, B. (2008): Recent progress in numerical methods for the Poisson-Boltzmann equation in biophysical applications. *Commun Comput Phys*, vol. 3, no. 5, pp. 973–1009.

Mitchell, A. R.; Griffiths, D. F. (1980): The finite difference method in partial differential equations: John Wiley.

Nishimura, N.; Liu, Y. (2004): Thermal analysis of carbon-nanotube composites using a rigid-line inclusion model by the boundary integral equation method. *Computational Mechanics*, vol. 35, no. 1, pp. 1–10.

Pozrikidis, C. (2011): Shear flow past slender elastic rods attached to a plane. *International Journal of Solids and Structures*, vol. 48, no. 1, pp. 137–143.

Reddy, J. N.; Gartling, D. K. (2011): The finite element method in heat transfer and fluid dynamics: CRC press.

Shen, G. (2009): Devices and chemical sensing applications of metal oxide nanowires. *Journal of Materials Chemistry*, vol. 19, no. 7, pp. 828–839.

Simonson, T. (2003): Electrostatics and dynamics of proteins. *Reports on Progress in Physics*, vol. 66, no. 5, pp. 737.

Telles, J.; Wrobel, L. (1984): Boundary element techniques. Theory and applications in engineering, Springer-Verlag, Berlin.

Tornberg, A. K.; Shelley, M. J. (2004): Simulating the dynamics and interactions of flexible fibers in Stokes flows. *Journal of Computational Physics*, vol. 196, no. 1, pp. 8–40.

Wang, H.; Yao, Z. (2013): Large-scale thermal analysis of fiber composites using a line-inclusion model by the fast boundary element method. *Engineering Analysis with Boundary Elements*, vol. 37, no. 2, pp. 319–326.